



**HAL**  
open science

# Numerical investigations of anisotropic structures of red blood cell aggregates on ultrasonic backscattering

Lenin Chinchilla, Curtis Armstrong, Rym Mehri, Alessandro S Savoia,  
Marianne Fenech, Emilie Franceschini

## ► To cite this version:

Lenin Chinchilla, Curtis Armstrong, Rym Mehri, Alessandro S Savoia, Marianne Fenech, et al.. Numerical investigations of anisotropic structures of red blood cell aggregates on ultrasonic backscattering. *Journal of the Acoustical Society of America*, 2021, 149 (4), pp.2415-2425. 10.1121/10.0003815 . hal-03357763

**HAL Id: hal-03357763**

**<https://hal.science/hal-03357763>**

Submitted on 30 Sep 2021

**HAL** is a multi-disciplinary open access archive for the deposit and dissemination of scientific research documents, whether they are published or not. The documents may come from teaching and research institutions in France or abroad, or from public or private research centers.

L'archive ouverte pluridisciplinaire **HAL**, est destinée au dépôt et à la diffusion de documents scientifiques de niveau recherche, publiés ou non, émanant des établissements d'enseignement et de recherche français ou étrangers, des laboratoires publics ou privés.

**Numerical investigations of anisotropic structures of red blood cell aggregates on ultrasonic backscattering**

Lenin Chinchilla,<sup>1</sup> Curtis Armstrong,<sup>2</sup> Rym Mehri,<sup>2</sup> Alessandro S. Savoia,<sup>3</sup> Marianne Fenech,<sup>4</sup> and Emilie Franceschini<sup>1, a)</sup>

<sup>1</sup>*Aix-Marseille Univ., CNRS, Centrale Marseille, LMA UMR 7031, Marseille, France*

<sup>2</sup>*University of Ottawa, Ottawa, Ontario, Canada*

<sup>3</sup>*Department of Engineering, Roma Tre University, 00146 Rome, Italy*

<sup>4</sup>*Department of Mechanical Engineering, University of Ottawa, Ottawa, Ontario, Canada*

(Dated: 6 February 2021)

1 Although quantitative ultrasound techniques based on the parameterization of  
2 the backscatter coefficient (BSC) have been successfully applied to blood charac-  
3 terization, theoretical scattering models assume blood as an isotropic scattering  
4 medium. However, the red blood cell (RBC) aggregates form anisotropic structures  
5 such as rouleaux. The present study proposes an anisotropic formulation of the  
6 Effective Medium Theory combined with the Local Monodisperse Approximation  
7 (EMTLMA) that considers perfectly aligned prolate-shaped aggregates. Theoretical  
8 BSC predictions were first compared with computer simulations of BSCs in a  
9 forward problem framework. Computer simulations were conducted for perfectly  
10 aligned prolate-shaped aggregates and more complex configurations with partially  
11 aligned prolate-shaped aggregates for which the size and orientation of RBC  
12 aggregates were obtained from blood optical observations. The isotropic and  
13 anisotropic EMTLMA models were then compared in an inverse problem framework  
14 to estimate blindly the structural parameters of RBC aggregates from the simulated  
15 BSCs. When considering the isotropic EMTLMA, the use of averaged BSCs over  
16 different insonification directions significantly improves the estimation of aggregate  
17 structural parameters. Overall, the anisotropic EMTLMA was found to be superior  
18 to the isotropic EMTLMA in estimating the scatterer volume distribution. These  
19 results contribute to a better interpretation of scatterer size estimates for blood  
20 characterization.

---

21  
a) [franceschini@lma.cnrs-mrs.fr](mailto:franceschini@lma.cnrs-mrs.fr)

22 **I. INTRODUCTION**

23 Quantitative UltraSound (QUS) techniques use the magnitude and frequency dependence  
24 of the backscatter spectrum from blood in order to obtain quantitative parameters reflect-  
25 ing the level of red blood cell (RBC) aggregation. A spectral analysis technique consists  
26 in estimating the spectral slope and intercept,<sup>1</sup> and was applied to estimate the size of the  
27 blood microstructure and the acoustic concentration (*i.e.*, the product of the scatterer con-  
28 centration times the square of the relative impedance difference between scatterers and the  
29 surrounding plasma medium).<sup>2</sup> Another QUS technique used to extract quantitative param-  
30 eters from aggregated RBC structures relies on theoretical backscattering models in order  
31 to fit the measured backscatter coefficient (BSC) by a theoretical BSC. The challenge is to  
32 develop suitable theoretical backscattering models that consider the high volume fraction  
33 occupied by RBCs in blood (named hematocrit) and the clustering of RBCs characterized  
34 by specific size and shape.<sup>4</sup> Two theoretical backscattering models have been developed:  
35 the Structure Factor Size Estimator (SFSE) and the Effective Medium Theory combined  
36 with the Structure Factor Model (EMTSFM). The SFSE theory approximates the structure  
37 factor with its second-order Taylor expansion and estimates two QUS parameters: the mean  
38 aggregate isotropic diameter and the packing factor.<sup>5,6</sup> However, these two QUS parameters  
39 were found to be correlated, reducing the BSC parameterization to one QUS parameter  
40 and making the SFSE theory difficult to interpret physically.<sup>5,7</sup> Despite this limitation,  
41 the SFSE theory was applied successfully to measure the RBC aggregation in relation to  
42 systemic inflammation in *in vivo* preclinical studies for varying circulatory disorders such

43 as deep vein thrombosis, cardiopulmonary bypass and diabetes.<sup>8</sup> The EMTSFM consists in  
44 treating the RBC aggregates as individual homogeneous scatterers and in calculating the  
45 backscattering from the collection of effective scatterers using the structure factor model.<sup>9</sup>  
46 In the case of polydisperse aggregate size, the effective medium theory can be combined  
47 with the polydisperse structure factor model for a gamma size distribution,<sup>10</sup> or combined  
48 with the Local Monodisperse Approximation (EMTLMA) for any size distribution.<sup>11</sup> The  
49 local monodisperse approximation is an approximation of the polydisperse structure fac-  
50 tor model, which is valid for moderate polydispersity.<sup>12</sup> The polydisperse EMTSFM (or  
51 equivalently the polydisperse EMTLMA) provides three QUS parameters: the mean and  
52 standard deviation of the aggregate size distribution and the aggregate compactness. Previ-  
53 ous three-dimensional (3D) computer simulations<sup>13</sup> and *in vitro* experiments on aggregating  
54 blood<sup>10,11</sup> demonstrated that the EMTSFM and EMTLMA were more suitable than the  
55 SFSE for characterizing RBC aggregation. The EMTSFM and EMTLMA models provide  
56 a straightforward physical interpretation of the QUS estimates, since the aggregate size  
57 distributions estimated by these models are consistent with the direct optical observations  
58 in controlled blood flow.<sup>10,11</sup>

59

60 All the aforementioned models (SFSE, EMTSFM and EMTLMA) assume that aggregates  
61 are spherical, so that blood is considered as an isotropic scattering medium. However, it is  
62 well known that RBC aggregates form anisotropic structures, such as rouleaux in healthy  
63 blood or ellipsoidal clumps in pathological blood.<sup>14,15</sup> Moreover, some *in vitro* ultrasonic  
64 studies on controlled blood flow reported angular-dependent backscatter intensity that sug-

gest an orientation of the anisotropic aggregate structures with the flow streamlines.<sup>16,17,32</sup> In the presence of anisotropic aggregate structures, backscattering models considering spherical aggregates may create a bias against the QUS estimates.

68

The aims of the present study are:

- to propose an anisotropic formulation of the EMTLMA for modeling perfectly aligned prolate-shaped aggregates to better interpret anisotropic backscatter of aggregating blood, and
- to evaluate both isotropic and anisotropic EMTLMA to determine the structural features of anisotropic RBC aggregates from the measured BSCs.

There is no means to experimentally determine the RBC aggregate size and shape at a normal physiological hematocrit of 40%, because blood is opaque to light. The use of optical methods to assess the RBC aggregate structures is limited to measurements in 2D confined flows ( $<100\ \mu\text{m}$ ) and in cases of low hematocrits ( $<20\%$ ).<sup>10,23,24</sup> Whereas ultrasonic measurements of BSCs at 40 MHz, for instance, require the backscattered signal to be studied over an analysis window of at least 10 wavelengths ( $\approx 385\ \mu\text{m}$ ), which is much larger than microchip or rheometer gap used to observe dynamics of RBC aggregates in optical microscopy. This is why only qualitative comparisons between ultrasonic and optical measurements have been carried out so far.<sup>5,10</sup> The present study examines the anisotropic formulation of the EMTLMA and compares the use of this model to the isotropic EMTLMA from controlled computer simulations, where structural properties of RBC aggregates (size,

86 shape, orientation) are known. Computer simulations were carried out for two different  
 87 aggregating configurations: perfectly aligned prolate-shaped aggregates and more complex  
 88 configurations with partially aligned prolate-shaped aggregates. The complex aggregation  
 89 configurations correspond to the actual size and orientation distributions of aggregated RBCs  
 90 obtained from optical measurements of sheared blood in a microfluidic chip. First, the  
 91 BSC theoretical predictions given by the anisotropic EMTLMA are compared to simulated  
 92 BSCs, which are obtained from 3D computer simulations in the framework of a forward  
 93 problem study (*i.e.*, the theoretical BSCs were determined from known structural properties  
 94 of RBC aggregates). Second, the isotropic and anisotropic EMTLMA models are compared  
 95 in the inverse problem framework to estimate blindly the structural parameters of RBC  
 96 aggregates from the simulated BSCs. The ability of the two models (isotropic and anisotropic  
 97 EMTLMA) as means of determining the aggregate size distribution is finally discussed.

## 98 II. ULTRASOUND BACKSCATTERING THEORY

### 99 A. Differential backscattering cross-section modeling for a single aggregate

100 The effective medium theory assumes that aggregates of RBCs can be treated as indi-  
 101 vidual homogeneous scatterers, which have effective properties determined by the aggregate  
 102 compactness  $\phi_i$  and acoustic properties of plasma and RBCs.<sup>9,18</sup> The aggregate compactness  
 103 is defined as the volume fraction of RBCs within an aggregate. As a first approximation,  
 104 it is assumed that all the deformable RBCs are tightly compact within the aggregates, so  
 105 that the compactness  $\phi_i$  is equal to 1 for all aggregates. Therefore, the acoustic properties

106 of an aggregate (*i.e.*, compressibility  $\kappa$  and density  $\rho$ ) are those of the RBCs. To consider  
 107 the anisotropic structure of an aggregate, its shape is approximated by a prolate ellipsoid  
 108 having a semi-minor axis  $b$  and a semi-major axis  $\nu b$  (with  $\nu$  defined as the axial ratio). The  
 109 differential backscattering cross section  $\sigma$  of a prolate-shaped aggregate is given by:<sup>19</sup>

$$\sigma(k) = \frac{k^4(\gamma_\kappa - \gamma_\rho)^2}{16\pi^2} V^2 F(k) \quad (1)$$

110 where  $k$  is the wavenumber,  $V = \frac{4}{3}\pi\nu b^3$  the aggregate volume,  $\gamma_\kappa$  the relative contrast in  
 111 compressibility  $\gamma_\kappa = (\kappa - \kappa_0)/\kappa_0$  and  $\gamma_\rho$  the relative contrast in density  $\gamma_\rho = (\rho - \rho_0)/\rho$ ,  
 112 where  $\kappa_0$  and  $\rho_0$  are the compressibility and density of plasma, respectively. The ellipsoidal  
 113 form factor  $F(k)$  is defined as:<sup>20</sup>

$$F(k) = \left( \frac{3(\sin(2ku) - 2ku \cos(2ku))}{(2ku)^3} \right)^2, \quad (2)$$

$$\text{with } u = b\sqrt{1 + (\nu^2 - 1)\cos^2\theta},$$

114 where  $\theta$  is the relative orientation of ellipsoid, defined as the angle between the incident  
 115 wave direction and the major axis of the prolate ellipsoid.

## 116 **B. Effective Medium Theory combined with the Local Monodisperse Approxima-** 117 **tion (EMTLMA)**

118 The effective medium theory is combined with the local monodisperse approximation  
 119 to consider the interference effects caused by correlations between the spatial positions of  
 120 effective prolate ellipsoids (*i.e.*, the coherent scattering).<sup>11</sup> As a first approximation, it is  
 121 assumed that all the prolate ellipsoids have identical axial ratio  $\nu_f$ , that all the prolate  
 122 ellipsoids are aligned in the same fixed direction  $\theta_f$  and that their major axes are placed in

123 the  $\mathbf{xy}$  plane, as illustrated in Fig. 1. This configuration corresponds to aggregates aligned  
 124 in the flow streamlines. The orientation angle  $\alpha_f$  for a prolate ellipsoid is defined as the  
 125 angle between its major axis and the  $\mathbf{y}$  axis (rf. Fig. 1). One has  $\alpha_f = \pi/2 - \theta_f - \beta$  so that  
 126 either  $\alpha_f$  or  $\theta_f$  can be used to describe the prolate ellipsoid orientation.

127 The EMTLMA approximates the set of polydisperse prolate ellipsoids perfectly aligned  
 128 by a set of non-interacting monodisperse subsystems. For each monodisperse subsystem,  
 129 each scatterer with specific semi-minor axis  $b$ , axial ratio  $\nu_f$  and orientation  $\theta_f$  is assumed  
 130 to be surrounded by scatterers with identical characteristics. Thus, the BSC is computed  
 131 as the sum of the backscattering from monodisperse subsystem weighted by the probability  
 132 density function PDF of the semi-minor axis  $b$  (denoted  $p(b)$ ) as:

$$BSC_{\text{aniso}}(k) = m \int_0^{\infty} p(b) \sigma(k, b, \nu_f, \theta_f) S(k, u, \phi) db \quad (3)$$

133 where  $m$  is the number density of effective prolate ellipsoids,  $\sigma$  is the differential backscat-  
 134 tering cross-section given by Eq. (1), and  $S$  is the monodisperse structure factor for an  
 135 equivalent system, consisting only of particles of radius  $u$  with a fixed total volume fraction  
 136  $\phi$  occupied by the prolate ellipsoids. An analytical expression of the structure factor can  
 137 be obtained by using the Percus-Yevick approximation as established by Wertheim<sup>21</sup> and is  
 138 given by Eqs. (A1)-(A4) in Ref. 20.

139

140 For the peculiar case of polydisperse aggregates with spherical shape, the BSC using the  
 141 isotropic EMTLMA is expressed as:

$$BSC_{\text{iso}}(k) = m \int_0^{\infty} p(r) \sigma(k, r) S(k, r, \phi) dr, \quad (4)$$

142 where  $\sigma(k, r)$  is the backscattering cross section of a spherical aggregate of radius  $r$  given  
 143 by Eq. (1) by using  $\nu = 1$  and  $r=b$ .

### 144 III. MATERIAL AND METHODS

#### 145 A. Experiments on human blood sheared in microfluidic shearing system

146 Size and orientation distributions of RBC aggregates were obtained from experiments  
 147 described in Refs. 23 and 24. These experiments are briefly summarized here. Two human  
 148 blood samples (denoted A and B) were collected from two different healthy volunteers with  
 149 the approval of the ethics committee of the University of Ottawa (H11-13-06). The blood  
 150 was prepared following standard procedures as previously described.<sup>24</sup> Human RBCs were  
 151 then re-suspended in their respective plasma at an hematocrit of 10%. The RBC suspen-  
 152 sions were flowed and observed *in vitro* in a two-fluid flow poly-di-methyl-siloxane (PDMS)  
 153 microfluidic shearing system (see Fig. 1 in Ref. 24). The channel dimension is 120  $\mu\text{m}$  in  
 154 width and 60  $\mu\text{m}$  in height. Within this system, the RBC aggregates were entrained using  
 155 a second solution of phosphate buffered saline in order to obtain a linear velocity profile  
 156 within the blood layer and thus achieve a wide range of constant shear rates. The shear  
 157 rate was determined using a micro Particle Image Velocimetry ( $\mu\text{PIV}$ ) system (FlowMaster  
 158 MITAS, LaVision, USA), while RBC aggregates were simultaneously visualized by bright  
 159 field microscopy and recorded with a high speed camera (Basler acA2000-340kmNIR). Fi-  
 160 nally, the contours of approximately 400 aggregates were segmented manually on several

161 images. Each RBC aggregate contour is then fitted by an ellipse to obtain its semi-minor  
 162 axis, semi-major axis and orientation.

### 163 B. Computer simulations based on the Structure Factor Model

164 Computer simulations based on the Structure Factor Model (SFM) were conducted to  
 165 obtain the simulated  $BSC_{\text{sim}}$  from different aggregating configurations. First, polydisperse  
 166 prolate ellipsoids perfectly aligned were simulated, as illustrated in Fig. 1. The prolate ellip-  
 167 soids have identical axial ratio  $\nu_f$  and their semi-minor axes  $b$  are gamma distributed in line  
 168 with the anisotropic EMTLMA. For a fixed mean semi-minor axis  $\bar{b}/a=2.5$ , we study several  
 169 structural configurations with varying axial ratios  $\nu_f$  (ranging from 1.5 to 2.5) and varying  
 170 semi-minor axis standard deviations  $\bar{b}$  (ranging from  $0.18a$  to  $0.75a$ ). Second, the complex  
 171 aggregate configurations were based on optical measurements obtained from microfluidic  
 172 experiments as described in subsection III A. The RBC aggregates were approximated by  
 173 prolate ellipsoids with semi-minor axes, axial ratios and orientations following the distribu-  
 174 tions of size and orientation obtained from optical image segmentation of RBC aggregates.

175 For each aggregation configuration studied, non-overlapping prolate ellipsoids (*i.e.*, non-  
 176 overlapping RBC aggregates) were randomly distributed in a simulated volume  $V_{\text{sim}}$  using a  
 177 Monte Carlo algorithm (see section II.B.A in Ref.<sup>27</sup>). The simulated volume is fixed to  $250$   
 178  $\times 250 \times 250 \mu\text{m}^3$ , and the hematocrit is fixed to 10% or 30%. The simulated  $BSC_{\text{sim}}$  was  
 179 obtained using the SFM as follows:

$$BSC_{\text{sim}}(k) = m \left\langle \frac{1}{N} \left| \sum_{j=1}^N \Phi(k) e^{-i2k\mathbf{n}\cdot\mathbf{r}_j} \right|^2 \right\rangle, \quad (5)$$

180 where  $m$  is the number density of prolate ellipsoids equal to  $N/V_{\text{sim}}$ ,  $\Phi$  is the backscattering  
 181 amplitude of  $j$ th prolate ellipsoid,  $\mathbf{r}_j$  is the location of the  $j$ th prolate ellipsoid and  $\mathbf{n}$  is  
 182 the unit vector in the direction of the incident field. The symbol  $\langle \rangle$  represents the ensemble  
 183 average. The total number of prolate ellipsoids  $N$  is calculated by forcing the prescribed  
 184 volume fraction to  $\phi = (\sum_{j=1}^N \frac{4\pi}{3} \nu_j b_j^3) / V_{\text{sim}}$ . The backscattering amplitude  $\Phi$  is defined  
 185 as  $\Phi^2(k) = \sigma(k)$ , where  $\sigma$  is given in Eq. (1). One simulated  $BSC_{\text{sim}}$  was computed by  
 186 averaging 100 realizations for averaging purposes.

187 The simulated  $BSC_{\text{sim}}$  were performed with thirteen different insonification angles  $\beta$   
 188 ranging from  $-30^\circ$  to  $30^\circ$  with a step of  $5^\circ$ . In the case of perfectly aligned prolate ellipsoids,  
 189 the insonification angle  $\beta=0^\circ$  corresponds to the angle for which the major axis direction  
 190 of the prolate ellipsoids and the incident field direction are perpendicular. (This specific  
 191 direction of the major axis of the aligned prolate ellipsoids was arbitrarily chosen.) Examples  
 192 are shown in Fig. 2(a), where simulated  $BSC_{\text{sim}}$  were calculated for perfectly aligned prolate  
 193 ellipsoids ( $\phi=30\%$ ,  $\bar{b}/a=2.5$ ,  $\sigma_b/a=0.75$ ,  $\nu_f=2$ ) for different insonification angles  $\beta$ . A change  
 194 of BSC magnitude regarding different insonification angles  $\beta$  can be observed.

### 195 C. QUS parameter estimation

196 The measured BSCs with different insonification angles bring information on the anisotropy  
 197 of the scattering medium. For each insonification angle  $\beta$ , the  $iBSC$  is computed in the  
 198 wavenumber range of  $k_1$  to  $k_2$  as follows:

$$iBSC(\beta) = \frac{1}{(k_2 - k_1)} \int_{k_1}^{k_2} 10 \log_{10}(BSC(k, \beta)) dk. \quad (6)$$

199 The example of *iBSC* given in Fig. 2(b) suggests that the *iBSC* is highest when the  
 200 acoustic beam is perpendicular (normal) to the aligned structures, and the magnitude of  
 201 *iBSC* symmetrically decreases about the angle of normal incidence.<sup>28</sup> We evaluate the level  
 202 of anisotropy by measuring the difference between the maximum and minimum values of  
 203 *iBSC*( $\beta$ ), denoted  $D_{iBSC}$  (rf. Fig. 2(b)). The orientation  $\theta_f$  of the aligned structures can be  
 204 obtained by fitting a quadratic function  $h(\beta) = c_2\beta^2 + c_1\beta + c_0$  to the measured *iBSC*( $\beta$ ) (rf.  
 205 Fig. 2(b)). The location of the axis of symmetry of the quadratic function at  $\beta_0 = -c_1/(2c_2)$   
 206 gives the incident wave direction perpendicular to the axis of alignment of the ellipsoids. It  
 207 can be deduced that  $\alpha_f = -\beta_0$ , or equivalently  $\theta_f = \pi/2 - \alpha_f - \beta$ .

208 The QUS structural parameters are estimated by fitting the simulated  $BSC_{\text{sim}}$  with the  
 209 theoretical EMTLMA, and by assuming that the hematocrit  $\phi$ , the RBC radius  $a$  and the  
 210 acoustical properties of plasma and RBCs are known *a priori*. The parameter estimation  
 211 was carried out in the 10-42 MHz frequency bandwidth, which corresponds to the frequency  
 212 range used in a previous *in vitro* experimental study.<sup>10</sup> The main orientation of the aligned  
 213 structures is first determined as described previously, and the unknown parameters (mean  
 214 semi-minor axis  $\bar{b}^*$  with standard deviation  $\sigma_b^*$ , and axial ratio  $\nu_f^*$ ) are determined by min-  
 215 imizing the cost function  $\mathcal{F}$ , which synthesizes the thirteen simulated  $BSC_{\text{sim}}$  with the  
 216 thirteen insonification angles over the wavenumbers  $k_j$  in the wavenumber range of  $k_1$  to  $k_2$ :

$$\mathcal{F} = \frac{1}{M} \sum_{i=1}^M \frac{\sum_j \|BSC_{\text{sim}}(k_j, \theta_i) - BSC_{\text{aniso}}(k_j, \theta_i)\|^2}{\sum_j \|BSC_{\text{sim}}(k_j, \theta_i)\|^2}, \quad (7)$$

217  
 218 where  $M$  is the number of insonification angles (here  $M=13$ ) and  $BSC_{\text{aniso}}$  corresponds to  
 219 the anisotropic EMTLMA given by Eq. (3).

220 Finally, the isotropic EMTLMA was also employed to assess its ability of evaluating  
 221 the QUS parameters in anisotropic aggregating configurations. In that case, the isotropic  
 222 EMTLMA is fit to one single simulated  $BSC_{\text{sim}}$ : the  $BSC_{\text{sim}}$  averaged over the thirteen  
 223 insonification angles (denoted  $\overline{BSC(\beta)}$ ), or the single  $BSC_{\text{sim}}$  at the insonification angle  
 224  $\beta=0^\circ$ . The unknown parameters (mean radius  $\bar{r}^*$  with standard deviation  $\sigma_r^*$ ) are determined  
 225 by minimizing the relative mean error between one single  $BSC_{\text{sim}}$  and the theoretical  $BSC_{\text{iso}}$   
 226 given by Eq. (4).

227 Whatever the model used (isotropic or anisotropic), the routine *fmincon* of MATLAB  
 228 was employed to minimize the cost function  $\mathcal{F}$ , with the constraint  $p(r_{\text{eq}} < a_{\text{min}}) = 0$  (*i.e.*, the  
 229 equivalent aggregate radius should be larger than  $a_{\text{min}} = 1.82 \mu\text{m}$ ). The value  $a_{\text{min}}$  corresponds  
 230 to the minimum radius of sphere having the equivalent volume of a RBC in the segmented  
 231 images shown in Fig. 4(a). (This value is discussed in the Section VC.)

## 232 IV. RESULTS

### 233 A. Forward problem: comparison between simulated and theoretical BSCs

234 The aim was to compare the simulated  $BSC_{\text{sim}}$  and the theoretical  $BSC_{\text{theo}}$  in a large  
 235 frequency bandwidth of 10-70 MHz using the EMTLMA in the framework of the forward  
 236 problem study (*i.e.*, determining the BSCs from known distributions of aggregate shape, size  
 237 and orientation using the SFM and EMTLMA). The relative error in  $BSC_{\text{theo}}$  was calculated  
 238 over the 10-70 MHz frequency range as follows:  $\epsilon(k) = ||BSC_{\text{sim}}(k) - BSC_{\text{theo}}(k)|| / BSC_{\text{sim}}(k)$ .

239 **1. Perfectly aligned prolate ellipsoids**

240 Polydisperse aligned prolate ellipsoids were studied with identical mean semi-minor axis  
 241  $\bar{b}/a=2.5$ , and varying  $\sigma_b/a=0.18, 0.35$  or  $0.75$ , and  $\nu_f=2.0$  or  $2.5$  (rf. Fig. 3). As  $\nu_f$  increases,  
 242 the volume of scatterers increase, and, as a consequence, the  $BSC_{\text{sim}}$  amplitude increases at  
 243 low frequencies (before the first peak occurrence) and the first peak of the  $BSC_{\text{sim}}$  occurs at  
 244 lower frequencies (rf. Fig. 3(a)). As  $\sigma_b/a$  increases, the  $BSC_{\text{sim}}$  peaks are less pronounced  
 245 and the  $BSC_{\text{sim}}$  amplitude increases at low frequencies (rf. Fig. 3(b)).

246 When the  $BSC_{\text{sim}}$  are compared angle by angle, the first peak of the  $BSC_{\text{sim}}$  occurs at  
 247 higher frequencies when  $\sigma_b/a$  decreases, as expected (rf. Fig. 3(b)). For instance, for the  
 248 insonification angle  $\beta=30^\circ$ , the frequency at which the first peak of the  $BSC_{\text{sim}}$  occurs is 34  
 249 MHz with  $\sigma_b/a=0.75$ , and is 40 MHz with  $\sigma_b/a=0.18$ .

250 It is noticed that the dynamic range of BSC magnitude increases as the axial ratio  $\nu_f$   
 251 increases (rf. Figs. 3(a) and 3(c)). The changes in BSC magnitude at different insonification  
 252 angles are well pronounced in the high frequencies ( $>42\text{MHz}$ ) in all the cases studied, but  
 253 these changes are less pronounced in lower frequencies as the polydispersity decreases (rf.  
 254 Fig. 3(b)). Therefore, the difference between the maximum and minimum values of  $iBSC(\beta)$   
 255 ( $D_{iBSC}$ ) is less than 0.46 dB for  $\sigma_b/a \leq 0.45$ , against  $D_{iBSC} \approx 1.49$  dB for  $\sigma_b/a=0.75$  (rf. Fig.  
 256 3(c)). One can observe that, in the majority of the cases studied, the  $iBSC$  is highest at  
 257  $\beta=0$ , when the acoustic beam is perpendicular to the aligned structures (rf. Fig. 3(c)). In  
 258 the case ( $\sigma_b/a=0.18, \nu_f=2.0$ ), the  $iBSC$  is lowest at  $\beta=0^\circ$  because the peaks of  $BSC_{\text{sim}}$

occurs at higher frequencies for the smallest  $\sigma_b/a$ , so the  $BSC_{\text{sim}}$  are similar to within 0.5 dB for frequencies less than 42 MHz.

Also plotted in Figs. 3(a) and 3(b) are the theoretical  $BSC_{\text{aniso}}$  computed with the anisotropic EMTLMA given by Eq. (3) (solid lines). Satisfactory agreement was found between the simulation and the anisotropic EMTLMA theory with relative errors in  $BSC_{\text{aniso}}$  less than 22%, whatever the aggregating configuration studied for aligned prolate ellipsoids.

## 2. Complex aggregating configuration

A typical example of RBC aggregates flowing in two-fluid flow microfluidic shearing system, together with the corresponding contour segmentation, is shown in Fig. 4(a). Histograms of the distributions of the semi-minor axis, axial ratio, orientation and equivalent radius are represented in Figs. 4(b)-4(e) for both blood samples A and B. The equivalent radius  $r_{\text{eq}}$  corresponds to the sphere radius of equivalent volume to that of prolate ellipsoid. The semi-minor axis  $b$  and the equivalent radius of aggregate  $r_{\text{eq}}$  are normalized by the characteristic radius of a single RBC  $a=2.75 \mu\text{m}$ . These histograms correspond to the highest levels of aggregation obtained from each blood sample and were used as input data to obtain the simulated  $BSC_{\text{sim}}$ .

Figures (5a) and (5b) compares the simulated  $BSC_{\text{sim}}$  and the theoretical  $BSC_{\text{aniso}}$  when considering the complex aggregating configuration for the blood sample A at hematocrits of 10% and 30%. In line with the anisotropic EMTLMA proposed in section II B, the theoretical  $BSC_{\text{aniso}}$  considers the average axial ratio  $\bar{\nu}_f=2.7$  and the main aggregate orientation  $\alpha_f=-\beta_0=-7^\circ$  for  $\phi=10\%$  (and  $\alpha_f=-8^\circ$  for  $\phi=30\%$ ). The main orientation  $\alpha_f$  was estimated by

280 fitting the  $iBSC$  as a function of the insonification angle  $\beta$  (rf. Fig. 5(c)), and agrees  
 281 well with the maximum value of the histogram distribution of orientation (rf. Fig. 4).  
 282 One can observe that the theoretical anisotropic EMTLMA produces an overestimation  
 283 of the dynamic range of BSC magnitude when compared to the simulated  $BSC_{\text{sim}}$ . This  
 284 discrepancy will be discussed later in the Section V A.

## 285 B. Inverse problem: estimation of QUS parameters

286 In the following subsection, each given QUS parameter is the average over 10 QUS pa-  
 287 rameters estimated from 10 simulated  $BSC_{\text{sim}}$  in the same aggregating configuration. The  
 288 goodness-of-fit of the theoretical EMTLMA to the simulated  $BSC_{\text{sim}}$  was assessed by the  
 289 coefficient of determination.

290 Table II gives the mean values of QUS parameters estimated from the anisotropic and  
 291 isotropic EMTLMA for the aggregating configurations consisting in aligned prolate ellip-  
 292 soids. Also given in Table II are the  $D_{iBSC}$  and the goodness-of-fit statistic  $R^2$ . The  
 293 goodness-of-fit statistic  $R^2$  reveals that the anisotropic EMTLMA provides the best fit to  
 294 the  $BSC_{\text{sim}}$  curves ( $R^2 \geq 0.97$ ). For the largest polydispersity with  $\sigma_b/a=0.75$ , the isotropic  
 295 EMTLMA gives poorer fit curves with  $R^2$  comprised between 0.25 and 0.93. The smallest  
 296 value of  $R^2=0.25$  was obtained for the largest axial ratio  $\nu_f = 2.5$ , corresponding to the  
 297 largest value of  $D_{iBSC}$ . When considering the isotropic EMTLMA using  $\overline{BSC(\beta)}$ , the mean  
 298  $r_{\text{eq}}^*/a$  and  $\sigma_{\text{eq}}^*/a$  were estimated with relative errors less than 9% and 30%, respectively  
 299 (against relative errors up to 16% and 70% when considering the isotropic EMTLMA using  
 300  $BSC(\beta=0^\circ)$ ). When considering the anisotropic EMTLMA, the mean of QUS parameters

301 matched well the actual structural parameters with relative errors less than 3% for  $\bar{b}/a$ , 9%  
 302 for  $\sigma_b/a$  and 4% for  $\nu_f$ , by excluding the case of aligned prolate ellipsoids with  $\sigma_b/a=0.35$   
 303 and  $\nu_f=2$  (rf. Table II line 5). For this particular case, which corresponds to the smallest  
 304 level of anisotropy (*i.e.*, the smallest value of  $D_{iBSC}$ ), the relative errors of the estimates are  
 305 higher: up to 20% for the estimated  $\sigma_b^*/a$ . Figure 6 gives some examples of histograms of  
 306  $r_{eq}^3 p(r_{eq})$  estimated by the anisotropic or isotropic EMTLMA. The histograms of  $r_{eq}^3 p(r_{eq})$   
 307 are represented because the backscattering amplitude is proportional to the scatterer vol-  
 308 umes (and not the scatterer sizes). Overall, the aggregate volume distributions estimated  
 309 by the anisotropic EMTLMA match better the actual volume distribution when compared  
 310 to the isotropic EMTLMA.

311 Table III gives the mean values of QUS parameters estimated from the anisotropic and  
 312 isotropic EMTLMA for hematocrits of 10% and 30% when considering the complex aggre-  
 313 gating configurations with blood samples A and B. The isotropic EMTLMA using  $\overline{BSC}(\beta)$   
 314 had the best fit to the data with goodness-of-fit statistics  $R^2 \geq 0.95$ , against the anisotropic  
 315 EMTLMA giving  $R^2$  comprised between 0.85 and 0.93. When considering the isotropic  
 316 EMTLMA using  $\overline{BSC}(\beta)$ , mean sizes and standard deviations were estimated with relative  
 317 errors less than 18% and 8%, respectively (against relative errors less than 8% and 58% when  
 318 considering the isotropic EMTLMA using  $BSC(\beta=0^\circ)$ ). When considering the anisotropic  
 319 EMTLMA, the estimated equivalent radii were also computed as  $r^*=b^* \sqrt[3]{\nu_f^*}$ . In that case,  
 320 the mean size and standard deviation of  $r^*/a$  were estimated with relative errors less than  
 321 13% and 9%, respectively. Overall, the anisotropic EMTLMA largely underestimates the  
 322 mean axial ratio  $\bar{\nu}$  with relative errors up to 93%. Examples of histograms of  $r_{eq}^3 p(r_{eq})$

323 are given in Fig. (7). The scatterer volume PDFs estimated by the anisotropic EMTLMA  
 324 and by the isotropic EMTLMA using  $\overline{BSC(\beta)}$  are similar. Note that, in the case of the  
 325 blood sample B, the value of  $D_{iBSC}$  is the smallest (less than 0.75 dB), and the anisotropic  
 326 EMTLMA estimates an axial ratio  $\nu_f$  equal to 1 (*i.e.*, isotropic medium). That is why the  
 327 isotropic and anisotropic models gave identical scatterer volume PDF in that case (rf. Fig.  
 328 7(b)).

329 Note that the mean and standard deviation of the QUS parameters are given in supple-  
 330 mental Tables<sup>29</sup> for all aggregating configurations studied.

## 331 V. DISCUSSION AND CONCLUSION

### 332 A. On the assumption of perfectly aligned aggregates when using the anisotropic 333 EMTLMA

334 The anisotropic EMTLMA was developed to model perfectly aligned prolate ellipsoids  
 335 with identical axial ratio. Based on this modeling, the angle dependent BSCs from aggre-  
 336 gated RBCs were parameterized by four QUS parameters: the orientation  $\alpha_f$ , the axial  
 337 ratio  $\nu_f$ , and the mean  $\bar{b}^*$  and standard deviation  $\sigma_b^*$  of the semi-minor axis PDF. Both  
 338 assumptions of identical axial ratio and perfect alignment of aggregates allows us to reduce  
 339 the number of unknown QUS parameters, but they do not reflect the reality of rouleaux  
 340 structures as observed in the histograms of Figs. 4(c) and 4(d). Therefore, the anisotropic  
 341 EMTLMA modeling is not sufficient to model the backscattering from complex anisotropic  
 342 aggregates, as shown previously Figs. 5(a) and 5(b).

343 To better understand these discrepancies, it is necessary to study the effect of fixed  
 344 axial ratio  $\nu_f$  and/or fixed aggregate orientation  $\alpha_f$  on the BSC. In that aim, additional  
 345 computer simulations were performed to compute the  $BSC_{\text{sim}}$  from blood sample A at  
 346 hematocrit  $\phi=10\%$  by considering the joint PDF of  $b$ ,  $\nu$  and  $\alpha$  with a fixed  $\nu_f=2.7$  (denoted  
 347  $p(b, \nu_f, \alpha)$ ) and/or with a fixed  $\alpha_f=7^\circ$  (denoted  $p(b, \nu, \alpha_f)$ ). Figure 8 compares simulated  
 348  $BSC_{\text{sim}}$  by using the aggregate features of blood sample A and by considering different joint  
 349 PDFs:  $p(b, \nu, \alpha)$ ,  $p(b, \nu_f, \alpha)$ ,  $p(b, \nu, \alpha_f)$  and  $p(b, \nu_f, \alpha_f)$ . Note that the joint PDF  $p(b, \nu, \alpha)$   
 350 gives the true simulated  $BSC_{\text{sim}}$  (as already plotted in Fig. 5) and serves as reference data.  
 351 One can observe that the fixed  $\alpha_f$  produces a large overestimation of dynamic range of the  
 352  $BSC_{\text{sim}}$  magnitude, whereas the fixed  $\nu_f$  does not produce a significant change in the  $BSC_{\text{sim}}$   
 353 magnitude. Similar observations were obtained for the blood sample B (data not shown).  
 354 Therefore, the assumption of perfectly aligned prolate-shaped aggregate mainly causes the  
 355 discrepancies between simulated  $BSC_{\text{sim}}$  and theoretical  $BSC_{\text{aniso}}$  for the two blood samples  
 356 considered in this study.

357 In addition, this extensive forward problem study allows us to better understand the  
 358 estimates of QUS parameters. Indeed, the axial ratio  $\nu_f$  is always largely underestimated,  
 359 as shown in Table III. Let recall that the decrease in  $\nu_f$  has the effect of decreasing the  $D_{iBSC}$ ,  
 360 as shown in Fig. 3(a). Since the assumption of a fixed  $\alpha_f$  has the effect of overestimating  
 361 the  $D_{iBSC}$ , it goes with the underestimation of  $\nu_f$ .

## B. QUS parameters estimated by the isotropic and anisotropic EMTLMA

When considering perfectly aligned prolate-shaped aggregates, the anisotropic EMTLMA was found to be superior to the isotropic EMTLMA for characterizing scatterer volume distribution (rf. Fig. 6). The large differences between actual and estimated QUS parameters were obtained when the isotropic EMTLMA using  $BSC(\beta=0^\circ)$  was used to fit the measured data. However, it is interesting to observe that the mean scatterer radius matches quite well the expected radii (with relative errors less than 9%) when using the isotropic EMTLMA with  $\overline{BSC(\beta)}$ .

When considering the complex aggregating configurations with blood sample A, the anisotropic EMTLMA estimates the scatterer volume distribution more accurately than the isotropic EMTLMA (rf. Table III and Fig. 7). In that case, the mean radius  $\bar{r}^*/a$  underestimates the actual  $\bar{r}_{\text{eq}}/a$  with relative errors up to 13% when using the anisotropic EMTLMA, against relative errors up to 18% when using the isotropic EMTLMA. This underestimation of scatterer radius may be caused by the partial alignment of rouleaux, since the rouleaux structures are neither randomly oriented nor perfectly aligned.

Both anisotropic EMTLMA and isotropic EMTLMA using  $\overline{BSC(\beta)}$  yield quite similar scatterer volume distribution when considering complex aggregating configurations. Although the mean radius is slightly better estimated by the anisotropic EMTLMA, further aggregating configurations (with more varied sizes and orientations) need to be performed to evaluate the added value of anisotropic modeling. At present, the isotropic modeling (EMTLMA or EMTSFM) is fairly simple to implement and has proven its effectiveness in

383 estimating the scatterer volume distribution in previous experimental works on aggregating  
 384 blood.<sup>10,11</sup>

### 385 **C. Towards more realistic aggregating configurations in simulation**

386 In previous numerical studies, the ultrasonic backscattering of anisotropic RBC aggre-  
 387 gates was revealed by using simulated spatial arrangements of RBCs obtained from particle  
 388 dynamics<sup>25</sup> or statistical mechanics.<sup>26</sup> In those two-dimensional (2D) simulations, the size  
 389 and shape of RBC aggregates depend on the contribution of adhesive, repulsive and shear  
 390 forces set in the mechanical models. Although the resulting shapes visually resemble aggre-  
 391 gate of porcine RBCs, the elongation and orientation of anisotropic aggregates observed in  
 392 human blood cannot be reproduced with such simple models.<sup>30</sup> In the present study, the  
 393 structural characteristics (*i.e.* size, shape, orientation) of RBC aggregates were obtained  
 394 from optical measurements of blood sheared in a microfluidic chip. Then prolate-shaped  
 395 aggregates having these structural characteristics were randomly distributed within the sim-  
 396 ulated volume to compute the angular-dependent  $BSC_{\text{sim}}$ . To our knowledge, this is the  
 397 first time that actual size and orientation distributions of RBC aggregates obtained from  
 398 experiments are used for numerical simulations to study anisotropic backscatter in aggregat-  
 399 ing blood. However, the actual aggregate structures obtained in our microfluidic experiment  
 400 may differ from realistic conditions encountered in large blood vessels ( $\approx 1$  mm) at physiolog-  
 401 ical hematocrit, because of the experimental constraints for obtaining aggregate structures  
 402 by optical techniques as detailed below. First, the optical measurements were limited to a  
 403 low hematocrit of  $\phi = 10\%$ , because the RBCs are opaque to light. This opacity prevents

404 optical measurements at physiological hematocrit of 30-50%. So the simulations performed  
 405 at  $\phi = 30\%$  were based on the distributions of aggregate size and orientation measured at  
 406  $\phi = 10\%$ , whereas these distributions are expected to be different at  $\phi = 10\%$  and 30%. Sec-  
 407 ond, the two-fluid microfluidic shearing system has a small channel dimension of  $120 \mu\text{m} \times$   
 408  $60 \mu\text{m}$ , so aggregate sizes in this shearing system may be smaller than those encountered  
 409 in large blood vessels ( $\approx 1 \text{ mm}$ ). Third, the optical measurements give only access to two-  
 410 dimensional (2D) images of aggregates, so the aggregate shape was approximated by prolate  
 411 ellipsoid deduced from the fitted ellipse (see Fig. 4) and its major axis is assumed to be  
 412 placed in the  $\mathbf{xy}$  plane. This extrapolation of 2D information in 3D may also result in biases  
 413 on the polydispersity of the shape and orientation of the aggregates. For example, a single  
 414 RBC in 3D space is like an oblate ellipsoid of radii  $4.2 \mu\text{m}$ ,  $4.2 \mu\text{m}$  and  $1.2 \mu\text{m}$  (having the  
 415 equivalent volume of a sphere of radius  $a = 2.75 \mu\text{m}$ ), whereas the single RBC seen on the  
 416 edge in the 2D image is approximated by a prolate ellipsoid of radii  $4.2 \mu\text{m}$ ,  $1.2 \mu\text{m}$  and  $1.2$   
 417  $\mu\text{m}$  (having the equivalent volume of a sphere of radius  $a_{\min} = 1.82 \mu\text{m}$ ).

418 The histograms of the distributions of  $b$  and of  $\nu$  showed in Fig. 4 indicate that the  
 419 actual semi-minor axis does indeed follow a gamma PDF, but the axial ratio can vary in a  
 420 large range of values (from 1 up to 7). The histograms of the distributions of the aggregate  
 421 orientation demonstrate that the rouleaux spend more of their time quasi-aligned with the  
 422 flow streamlines, as observed in the pioneer work of Goldsmith.<sup>14</sup> Indeed, Fig. 4(d) indicates  
 423 that more than 39% of the aggregates in both blood samples have orientations  $\alpha = 0^\circ \pm 10^\circ$ ,  
 424 whereas, if the distribution were random, 16% of the aggregates would have this orientation.  
 425 It is interesting to notice that fitting the *iBSC* as a function of  $\beta$  was sufficient to estimate

426 satisfactorily the main orientation of aggregates, even if the aggregates are not perfectly  
 427 aligned.

428 Another interesting aspect concerning the actual orientation of aggregates (rf. Fig. 4(d))  
 429 is the fact that the distribution of orientations is similar for several studied blood samples  
 430 (data not shown for several blood samples). A deeper knowledge of the aggregate orientation  
 431 under various flow conditions (simple shear or tubular flow) would be useful to further  
 432 develop the anisotropic EMTLMA for estimating QUS parameters. For instance, one could  
 433 consider using *a priori* information on the distribution of aggregate orientation for the  
 434 anisotropic EMTLMA modeling, since the discrepancy between theoretical and simulated  
 435 BSCs when considering complex aggregating configurations is mainly due to the assumption  
 436 of perfectly aligned aggregates (as discussed in the Section V A).

#### 437 **D. Open questions to interpret the anisotropic ultrasonic backscattering from** 438 **sheared aggregating blood**

439 Several ultrasonic experiments<sup>16,17,31,32</sup> have been conducted to evaluate the angular-  
 440 dependence of backscattering of sheared RBC suspensions. At low shear rates promoting  
 441 the highest level of aggregation, the BSC magnitude is highest when the acoustic beam is  
 442 quasi-perpendicular to the velocity direction (see Figs. 3 and 5 in Ref.<sup>16</sup> for shear rate  $2 \text{ s}^{-1}$ ,  
 443 Fig. 7 in Ref.<sup>17</sup> for shear rate  $2 \text{ s}^{-1}$ , and Fig. 3 in Ref.<sup>31</sup> for shear rate  $3 \text{ s}^{-1}$ ). Our numerical  
 444 simulations from complex aggregating configurations (Fig. 5) are in good agreement with  
 445 these experiments. The anisotropic ultrasound signature (*iBSC* as a function of  $\beta$ ) could also

446 be used to obtain the main orientation of the aggregate structures with the flow streamlines  
447 (as discussed previously in subsection VC).

448 However, at moderate or high shear rates, the BSC magnitude (or the Doppler backscat-  
449 tered power) was also found to be the smallest when the acoustic beam is quasi-perpendicular  
450 to the velocity direction (see Fig. 6 in Ref.<sup>32</sup> in tubular flow for shear rates 17 - 51 s<sup>-1</sup>, see  
451 Fig. 3 in Ref.<sup>31</sup> in Couette flow for shear rates 25 - 140 s<sup>-1</sup>). This anisotropic ultrasound  
452 signature in U-shape is difficult to interpret, because it can be attributed to specific size and  
453 shape of RBC aggregates as simulated from the smallest standard deviation  $\sigma_b/a=0.18$  in  
454 Fig. 3c, or as hypothesized by Allard et al.<sup>32</sup> with cone-shaped structures. It may also be  
455 due to the shear-induced anisotropic microstructure, as observed in sheared suspensions of  
456 hard-spheres by Lombard et al.<sup>33</sup> Indeed, the spatial organisation (*i.e.*, the microstructure)  
457 of hard spheres in sheared concentrated suspensions shows a lower probability of finding  
458 pair of particles close to the velocity direction.<sup>34</sup> This region depleted in particles shows  
459 a higher ordering and thus influences greatly the magnitude of BSC and structure factor  
460 in the corresponding direction in the frequency domain.<sup>33</sup> If one considers the aggregate  
461 structures as effective scatterers, this region depleted in effective scatterers may explain the  
462 anisotropic ultrasound signature in U-shape reported in Refs.<sup>31</sup> and<sup>32</sup> at moderate or high  
463 shear rates. The numerical simulations performed in this study do not consider the shear-  
464 induced anisotropic microstructure, which is not yet understood in RBC suspensions.<sup>35</sup> In  
465 future experimental studies, exploring the use of a confocal microscope with ghost RBCs  
466 (*i.e.*, optically visible RBCs with no hemoglobin) to determine the microstructure, size and  
467 shape of RBC aggregates within larger microfluidic shearing systems could provide inval-

468 able information to fully understand the ultrasonic backscattering from anisotropic RBC  
 469 aggregates.

## 470 **E. Concluding remarks**

471 The present study contributes to the understanding of ultrasonic scattering from aggre-  
 472 gated RBCs and to the practical assessment of RBC aggregate size towards the monitoring  
 473 of inflammatory response in circulatory diseases. The following contributions were made in  
 474 this paper.

- 475 1. An anisotropic formulation of the EMTLMA was proposed to predict the angular-  
 476 dependent BSC from aligned prolate-shaped aggregates, assuming that the prolate-  
 477 shaped aggregates are perfectly aligned with the flow streamlines. Specifically, the  
 478 anisotropic EMTLMA considers the correlation among effective prolate ellipsoids (*i.e.*,  
 479 among aggregates) by using the anisotropic structure factor.
- 480 2. The anisotropic EMTLMA model, combined with numerical simulations taking into  
 481 account the joint PDF  $p(b, \nu, \alpha)$ , makes it possible to study the influence of specific  
 482 aggregate structure (polydispersity in terms of size, anisotropic aggregate shape and/or  
 483 orientation) on the BSC.
- 484 3. This numerical study sheds new light on the angular-dependent BSC data to be used  
 485 for a practical evaluation of RBC aggregate structures. The isotropic EMTLMA that  
 486 uses only the BSC perpendicular to the flow streamlines (which is the measurement  
 487 available in a conventional practical approach) presents important deviations from

488 the real aggregate size distribution. Whereas the isotropic EMTLMA that uses the  
489 averaged BSCs over different insonification directions provide satisfactory estimates.  
490 This shows that, for a practical evaluation of RBC aggregate structures, the use of  
491 averaged BSCs over different insonification directions can significantly improve the  
492 estimation of aggregate structural parameters, even if the model is biased. Overall,  
493 the anisotropic EMTLMA estimates the scatterer volume distribution more accurately  
494 than the isotropic EMTLMA; but further simulations with complex aggregating con-  
495 figurations (with more varied sizes and orientations) should be conducted to further  
496 evaluate the added value of anisotropic modeling for practical assessment of RBC  
497 structural features.

## 498 **ACKNOWLEDGMENTS**

499 This work was supported by the financial support of Grant No. ANR-15-CE19-0017  
500 and No. ANR-10-LABX-0092, and the Colombian department of Science and technology  
501 Colciencias.

## 502 **REFERENCES**

503 <sup>1</sup>F. L. Lizzi, M. Ostromogilsky, E. J. Feleppa, M. C. Rorke and M. M. Yaremko, “Re-  
504 lationship of ultrasonic spectral parameters to features of tissue microstructure,” IEEE  
505 transactions on ultrasonics, ferroelectrics, and frequency control **34**(3), 319–329 (1987).

- 506 <sup>2</sup>H. Kitamura, B. Sigel, J. Machi, E. J. Feleppa, J. Sokil-Melgar and J. Justin, “Roles  
507 of hematocrit and fibrinogen in red cell aggregation determined by ultrasonic scattering  
508 properties,” *Ultrasound in medicine & biology* **21**(6), 827–832 (1995).
- 509 <sup>3</sup>Y. Kurokawa, H. Taki, S. Yashiro, K. Nagasawa, Y. Ishigaki, and H. Kanai, “Estima-  
510 tion of size of red blood cell aggregates using backscattering property of high-frequency  
511 ultrasound: In vivo evaluation,” *Japanese Journal of Applied Physics* **55**(07KF12), 1–8  
512 (2016).
- 513 <sup>4</sup>L. Y. L. Mo and R. S. C. Cobbold, “Theoretical models of ultrasonic scattering in blood,”  
514 in *Ultrasonic Scattering in Biological Tissues*, edited by K. K. Shung and G. A. Thieme  
515 (CRC, Boca Raton, FL, 1993), Chap. 5, pp. 125-170.
- 516 <sup>5</sup>F. T. Yu and G. Cloutier, “Experimental ultrasound characterization of red blood cell ag-  
517 gregation using the structure factor size estimator,” *The Journal of the Acoustical Society*  
518 *of America* **122**(1), 645–656 (2007).
- 519 <sup>6</sup>F. T. Yu, E. Franceschini, B. Chayer, J. K. Armstrong, H. J. Meiselman, and G. Cloutier,  
520 “Ultrasonic parametric imaging of erythrocyte aggregation using the structure factor size  
521 estimator,” *Biorheology* **46**(4), 343–363 (2009).
- 522 <sup>7</sup>R. K. Saha, E. Franceschini, and G. Cloutier, “Assessment of accuracy of the structure-  
523 factor-size-estimator method in determining red blood cell aggregate size from ultrasound  
524 spectral backscatter coefficient,” *The Journal of the Acoustical Society of America* **129**(4),  
525 2269–2277 (2011).

- 526 <sup>8</sup>P. Gyawali, D. Ziegler, J.-F. Cailhier, A. Denault, and G. Cloutier, “Quantitative mea-  
527 surement of erythrocyte aggregation as a systemic inflammatory marker by ultrasound  
528 Imaging: a systematic review author links open overlay panel,” *Ultrasound in medicine &*  
529 *biology* **44**(7), 1303–1317 (2018).
- 530 <sup>9</sup>E. Franceschini, B. Metzger, and G. Cloutier, “Forward problem study of an effective  
531 medium model for ultrasound blood characterization,” *IEEE transactions on ultrasonics,*  
532 *ferroelectrics, and frequency control* **58**(12), 2668–2679 (2011).
- 533 <sup>10</sup>R. De Monchy, J. Rouyer, F. Destrempe, B. Chayer, G. Cloutier, and E. Franceschini,  
534 “Estimation of polydispersity in aggregating red blood cells by quantitative ultrasound  
535 backscatter analysis,” *The Journal of the Acoustical Society of America* **143**(4), 2207–  
536 2216 (2018).
- 537 <sup>11</sup>R. de Monchy, B. Chayer, G. Cloutier, and E. Franceschini, “Effective medium theory  
538 combined with a polydisperse structure factor model for characterizing red blood cell  
539 aggregation,” in *2016 IEEE International Ultrasonics Symposium (IUS)*, IEEE (2016),  
540 pp. 1–4.
- 541 <sup>12</sup>R. de Monchy, “Development and assessment of effective medium theory combined with  
542 polydisperse structure factor for the ultrasonic characterization of erythrocyte aggrega-  
543 tion,” Ph.D. thesis, Aix-Marseille, 2016.
- 544 <sup>13</sup>E. Franceschini, R. K. Saha, and G. Cloutier, “Comparison of three scattering models for  
545 ultrasound blood characterization,” *IEEE transactions on ultrasonics, ferroelectrics, and*  
546 *frequency control* **60**(11), 2321–2334 (2013).

- 547 <sup>14</sup>H. L. Goldsmith, “The microrheology of red blood cell suspensions,” *The Journal of general*  
548 *physiology* **52**(1), 5–28 (1968).
- 549 <sup>15</sup>O. Baskurt, B. Neu, and H. J. Meiselman, *Red blood cell aggregation*, Chap. 3, 31–62 (CRC  
550 Press, Boca Raton, FL).
- 551 <sup>16</sup>C. Guilbert, F. Yu, and G. Cloutier, “New observations on the anisotropy of ultrasound  
552 blood backscatter as a function of frequency and shear rate,” in *2007 IEEE International*  
553 *Ultrasonics Symposium (IUS)*, IEEE (2007), pp. 1013–1016.
- 554 <sup>17</sup>J. Garcia-Duitama, B. Chayer, A. Han, D. Garcia, M. L. Oelze, and G. Cloutier, “Experi-  
555 mental application of ultrafast imaging to spectral tissue characterization,” *Ultrasound in*  
556 *medicine & biology* **41**(9), 2506–2519 (2015).
- 557 <sup>18</sup>R. de Monchy, F. Destrempes, R. Saha, G. Cloutier, and E. Franceschini, “Coherent and  
558 incoherent ultrasound backscatter from cell aggregates,” *The Journal of the Acoustical*  
559 *Society of America* **140**(3), 2173–2184 (2016).
- 560 <sup>19</sup>M. F. Insana and D. G. Brown, “Acoustic scattering theory applied to soft biological  
561 tissues”, in *Ultrasonic Scattering in Biological Tissues*, edited by K. K. Shung and G. A.  
562 Thieme (CRC, Boca Raton, FL, 1993), Chap. 4, pp. 76–124.
- 563 <sup>20</sup>N. Saitô and Y. Ikeda, “The light scattering by non-spherical particles in solutions,” *Jour-*  
564 *nal of the Physical Society of Japan* **6**(5), 305–308 (1951).
- 565 <sup>21</sup>M. Wertheim, “Exact solution of the percus-yevick integral equation for hard spheres,”  
566 *Physical Review Letters* **10**(8), 321 (1963).

- 567 <sup>22</sup>E. Franceschini and R. Guillermin, “Experimental assessment of four ultrasound scattering  
568 models for characterizing concentrated tissue-mimicking phantoms,” *The Journal of the*  
569 *Acoustical Society of America* **132**(6), 3735–3747 (2012).
- 570 <sup>23</sup>R. Mehri, C. Mavriplis, and M. Fenech, “Design of a microfluidic system for red blood cell  
571 aggregation investigation,” *Journal of biomechanical engineering* **136**(6), 064501 (2014).
- 572 <sup>24</sup>R. Mehri, E. Niazi, C. Mavriplis, and M. Fenech, “An automated method for dynamic  
573 red blood cell aggregate detection in microfluidic flow,” *Physiological measurement* **39**(1),  
574 01NT02 (2018).
- 575 <sup>25</sup>I. Fontaine, D. Savery, and G. Cloutier, “Simulation of ultrasound backscattering by red  
576 cell aggregates: Effect of shear rate and anisotropy,” *Biophysical Journal* **82**(4), 1696–1710  
577 (2002).
- 578 <sup>26</sup>D. Savery and G. Cloutier, “Effect of red cell clustering and anisotropy on ultrasound blood  
579 backscatter: a monte carlo study,” *IEEE Transactions on Ultrasonics, Ferroelectrics, and*  
580 *Frequency Control* **52**(1), 94–103 (2005).
- 581 <sup>27</sup>R. K. Saha and G. Cloutier, “Monte carlo study on ultrasound backscattering by three-  
582 dimensional distributions of red blood cells,” *Physical review E* **78**(6), 061919 (2008).
- 583 <sup>28</sup>Q. W. Guerrero, I. M. Rosado-Mendez, L. C. Drehfal, H. Feltovich, and T. J. Hall, “Quan-  
584 tifying backscatter anisotropy using the reference phantom method,” *IEEE transactions*  
585 *on ultrasonics, ferroelectrics, and frequency control* **64**(7), 1063–1077 (2017).
- 586 <sup>29</sup>See supplementary material at [URL that will be inserted by AIP] for Tables showing the  
587 mean and standard deviations of the QUS parameters for all aggregating configurations.

- 588 <sup>30</sup>V. Claveria, C. Wagner, and P. Connes, “Aggregating and blood flow in health and disease”,  
589 in Dynamics of blood cell suspensions in microflows, edited by A. Villat and M. Abkarian  
590 (CRC, Boca Raton, FL, 2020), Chap. 6, pp. 183–213.
- 591 <sup>31</sup>J. Rouyer, L. Chinchilla, O. Lombard, and E. Franceschini, “Characterizing the erythro-  
592 cyte aggregation using the anisotropy of ultrasonic backscatter,” in *2018 IEEE Interna-*  
593 *tional Ultrasonics Symposium (IUS)*, IEEE (2018), pp. 1–4.
- 594 <sup>32</sup>L. Allard, G. Cloutier, and L.-G. Durand, “Effect of the insonification angle on the doppler  
595 backscattered power under red blood cell aggregation conditions,” *IEEE transactions on*  
596 *ultrasonics, ferroelectrics, and frequency control* **43**(2), 211–219 (1996).
- 597 <sup>33</sup>O. Lombard, J. Rouyer, E. Debieu, F. Blanc, and E. Franceschini, “Ultrasonic backscatter-  
598 ing and microstructure in sheared concentrated suspensions,” *The Journal of the Acous-*  
599 *tical Society of America* **147**(3), 1359–1367 (2020).
- 600 <sup>34</sup>F. Blanc, E. Lemaire, A. Meunier, and F. Peters, “Microstructure in sheared non-brownian  
601 concentrated suspensions,” *Journal of rheology* **57**(1), 273–292 (2013).
- 602 <sup>35</sup>L. Mountrakis, E. Lorenz, and A. G. Hoekstra, “Scaling of shear-induced diffusion and  
603 clustering in a blood-like suspension,” *Europhysics Letters* **114**14002 (2016).

604 FIGURE CAPTIONS

605  
606 Figure 1. (Color online) Schematic drawing of perfectly aligned prolate ellipsoids.

607  
608 Figure 2. (Color online) (a) Typical examples of simulated  $BSC_{\text{sim}}$  for perfectly aligned  
609 with  $\phi=30\%$ ,  $\bar{b}=2.5a=6.88 \mu\text{m}$ ,  $\sigma_b/a=0.75$  and  $\nu_f=2$ . The vertical dashed line indi-  
610 cates the frequency of 42 MHz. (b) Corresponding  $iBSC$  (symbols) in the 10-42 MHz  
611 frequency bandwidth as a function of different insonification angles  $\beta$ . Also plotted  
612 in dashed lines are the quadratic function  $h(\beta)$  used to estimate the main aggregate  
613 orientation.

614  
615 Figure 3. (Color online) (a) and (b) Comparison between simulated  $BSC_{\text{sim}}$  (symbols)  
616 and theoretical  $BSC_{\text{aniso}}$  (solid lines) at insonification angles  $\beta=0^\circ$  and  $30^\circ$  for aligned  
617 prolate ellipsoids with identical mean semi-minor axis  $\bar{b}/a=2.5$  of varying  $\nu_f$  (see panel  
618 a) and of varying  $\sigma/a$  (see panel b). The hematocrit is 30%. The vertical dashed lines  
619 indicate the frequency of 42 MHz. (c) Corresponding simulated  $iBSC$  (symbols) in  
620 the 10-42 MHz frequency bandwidth. Also plotted in dashed lines are the quadratic  
621 function  $h(\beta)$  used to estimate the main aggregate orientation.

622  
623 Figure 4. (a) Typical example of RBC aggregates flowing in two-fluid flow microfluidic  
624 shearing system. The aggregate contours are in green dashed lines and the correspond-  
625 ing fitted ellipses are in red solid lines. (b), (c), (d) and (e) Histogram distributions

626 of the semi-minor axis, axial ratio, orientation angle and equivalent radius for the two  
 627 blood samples studied.

628

629 Figure 5. (Color online) (a) Comparison between simulated  $BSC_{\text{sim}}$  (symbols) and  
 630 theoretical  $BSC_{\text{aniso}}$  (solid lines) at hematocrit  $\phi=10\%$  for complex aggregating config-  
 631 uration with blood sample A. (b) Same as (a) at hematocrit  $\phi=30\%$ . (c) Corresponding  
 632 simulated  $iBSC$  (symbols) in the 10-42 MHz frequency bandwidth. Also plotted in  
 633 dashed lines are the fitted quadratic function  $h(\beta)$ , its maximum being indicated by  
 634 the symbol x.

635

636 Figure 6. (Color online) Comparisons between actual and estimated histograms of  
 637  $r_{\text{eq}}^3 p(r_{\text{eq}})$  using the anisotropic or isotropic EMTLMA for the perfectly aligned prolate  
 638 ellipsoids  $\bar{b}/a=2.5$ ,  $\nu_f=2$  and varying  $\sigma_b$ .

639

640 Figure 7. (Color online) Comparisons between actual and estimated histograms of  
 641  $r_{\text{eq}}^3 p(r_{\text{eq}})$  using the anisotropic or isotropic EMTLMA for hematocrit of 10% when  
 642 considering the complex aggregating configurations with both blood samples A and B.

643

644 Figure 8. (Color online) Simulated  $BSC_{\text{sim}}$  for the complex aggregation configuration  
 645 using the aggregate features of blood sample A with  $\beta=0^\circ$  (losange symbols) and  $\beta=30^\circ$   
 646 (square symbols). The hematocrit is equal to 10%. Different joint PDFs are considered:  
 647  $p(b, \nu, \alpha)$ ,  $p(b, \nu_f, \alpha)$ ,  $p(b, \nu, \alpha_f)$  and  $p(b, \nu_f, \alpha_f)$ .

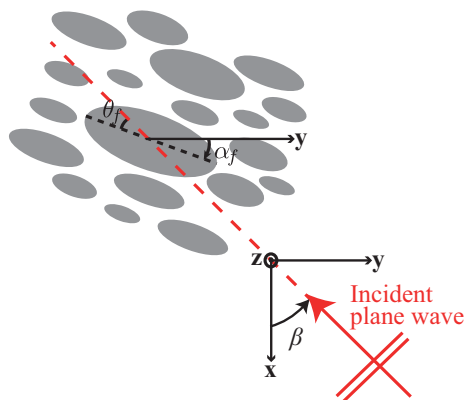


FIG. 1. (Color online) Schematic drawing of perfectly aligned prolate ellipsoids.

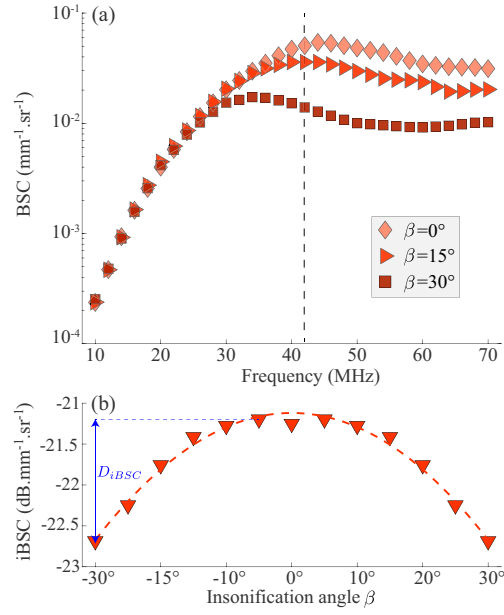


FIG. 2. (Color online) (a) Typical examples of simulated  $BSC_{\text{sim}}$  for perfectly aligned with  $\phi=30\%$ ,  $\bar{b}=2.5a=6.88 \mu\text{m}$ ,  $\sigma_b/a=0.75$  and  $\nu_f=2$ . The vertical dashed line indicates the frequency of 42 MHz. (b) Corresponding  $iBSC$  (symbols) in the 10-42 MHz frequency bandwidth as a function of different insonification angles  $\beta$ . Also plotted in dashed lines are the quadratic function  $h(\beta)$  used to estimate the main aggregate orientation.

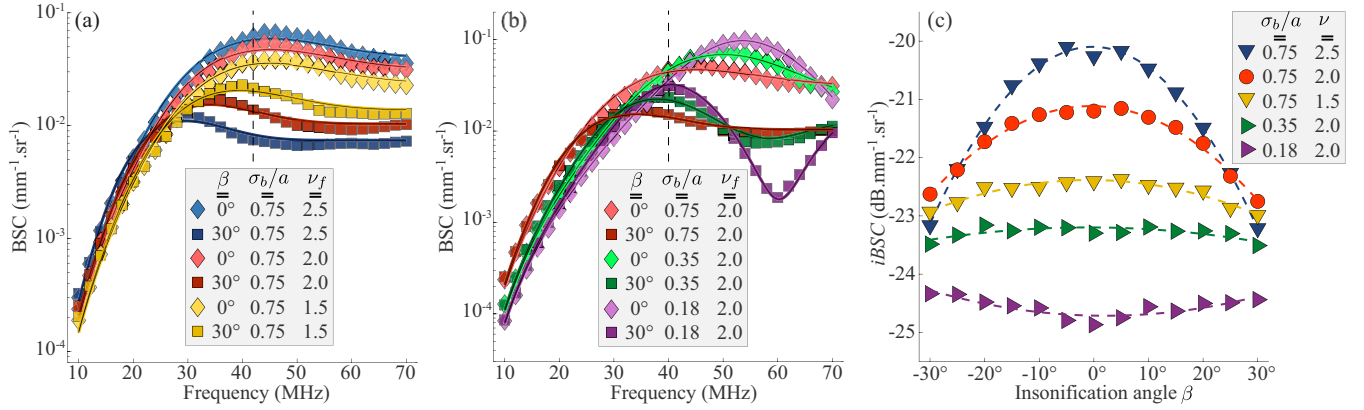


FIG. 3. (Color online) (a) and (b) Comparison between simulated  $BSC_{\text{sim}}$  (symbols) and theoretical  $BSC_{\text{aniso}}$  (solid lines) at insonification angles  $\beta=0^\circ$  and  $30^\circ$  for aligned prolate ellipsoids with identical mean semi-minor axis  $\bar{b}/a=2.5$  of varying  $\nu_f$  (see panel a) and of varying  $\sigma/a$  (see panel b). The hematocrit is 30%. The vertical dashed lines indicate the frequency of 42 MHz. (c) Corresponding simulated  $iBSC$  (symbols) in the 10-42 MHz frequency bandwidth. Also plotted in dashed lines are the quadratic function  $h(\beta)$  used to estimate the main aggregate orientation.

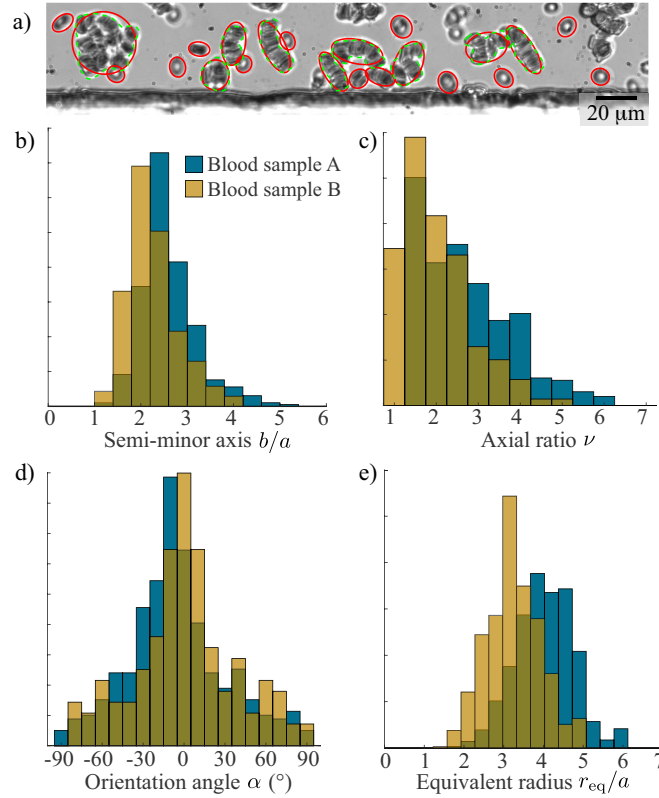


FIG. 4. (Color online) (a) Typical example of RBC aggregates flowing in two-fluid flow microfluidic shearing system. The aggregate contours are in green dashed lines and the corresponding fitted ellipses are in red solid lines. (b), (c), (d) and (e) Histogram distributions of the semi-minor axis, axial ratio, orientation angle and equivalent radius for the two blood samples studied.

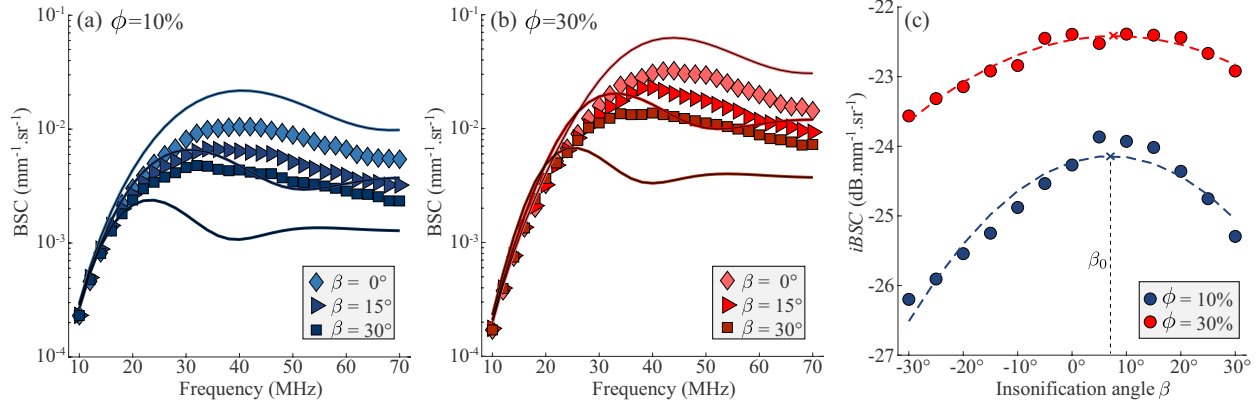


FIG. 5. (Color online) (a) Comparison between simulated  $BSC_{\text{sim}}$  (symbols) and theoretical  $BSC_{\text{aniso}}$  (solid lines) at hematocrit  $\phi=10\%$  for complex aggregating configuration with blood sample A. (b) Same as (a) at hematocrit  $\phi=30\%$ . (c) Corresponding simulated  $iBSC$  (symbols) in the 10-42 MHz frequency bandwidth. Also plotted in dashed lines are the fitted quadratic function  $h(\beta)$ , its maximum being indicated by the symbol x.

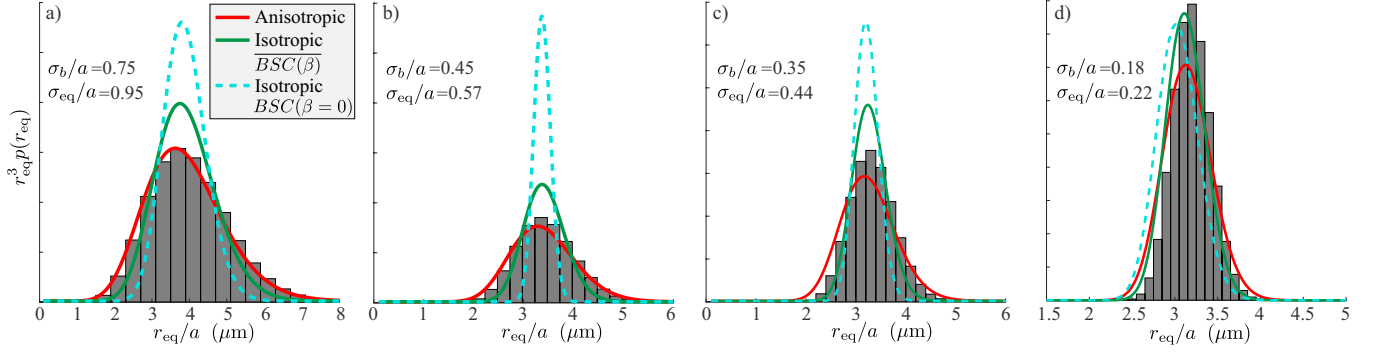


FIG. 6. (Color online) Comparisons between actual and estimated histograms of  $r_{\text{eq}}^3 p(r_{\text{eq}})$  using the anisotropic or isotropic EMTLMA for the perfectly aligned prolate ellipsoids  $\bar{b}/a=2.5$ ,  $\nu_f=2$  and varying  $\sigma_b$ .

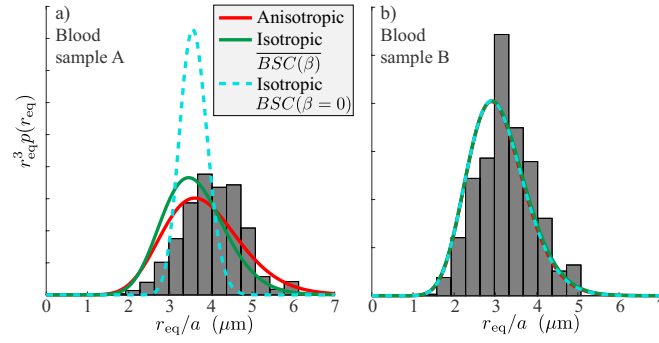


FIG. 7. (Color online) Comparisons between actual and estimated histograms of  $r_{\text{eq}}^3 p(r_{\text{eq}})$  using the anisotropic or isotropic EMTLMA for hematocrit of 10% when considering the complex aggregating configurations with both blood samples A and B.

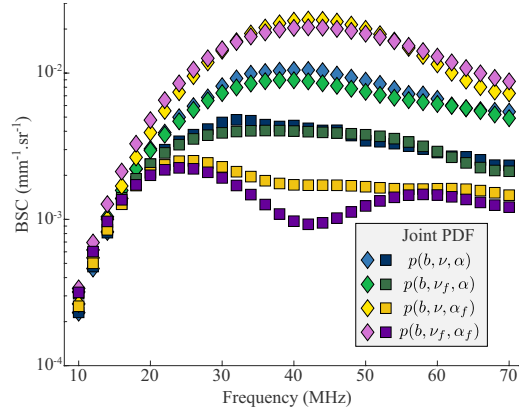


FIG. 8. (Color online) Simulated  $BSC_{\text{sim}}$  for the complex aggregation configuration using the aggregate features of blood sample A with  $\beta=0^\circ$  (losange symbols) and  $\beta=30^\circ$  (square symbols). The hematocrit is equal to 10%. Different joint PDFs are considered:  $p(b, \nu, \alpha)$ ,  $p(b, \nu_f, \alpha)$ ,  $p(b, \nu, \alpha_f)$  and  $p(b, \nu_f, \alpha_f)$ .

## 648 TABLE CAPTIONS

649

650 Table I. List of symbols.

651

652 Table II. The mean of QUS parameters estimated by the anisotropic or isotropic  
653 EMTLMA for the aggregating configurations consisting in perfectly aligned prolate  
654 ellipsoids at hematocrit  $\phi=30\%$ . Also given are the corresponding goodness-of-fit  $R^2$ .

655

656 Table III. The mean values of QUS parameters estimated by the anisotropic or isotropic  
657 EMTLMA for hematocrits of 10% and 30% when considering the complex aggregating  
658 configurations with blood sample A (see lines 1 and 2) and sample B (see lines 3 and  
659 4). Also given are the corresponding goodness-of-fit  $R^2$ .

TABLE I. List of symbols

---

$a$	radius of red blood cell
$b$	semi-minor axis of prolate ellipsoid
$\bar{b}$	mean semi-minor axis of prolate ellipsoid
$BSC_{\text{aniso}}$	backscatter coefficient of isotropic EMTLMA
$BSC_{\text{iso}}$	backscatter coefficient of anisotropic EMTLMA
$F$	ellipsoidal form factor
$k$	wavenumber
$m$	number density of effective prolate ellipsoids
$p(b)$	probability density function of semi-minor axis
$r$	radius of spherical aggregate
$r_{\text{eq}}$	sphere radius of equivalent volume to that of prolate ellipsoid
$S$	structure factor
$V$	aggregate volume
$\alpha$	angle between major axis of prolate ellipsoid and $\mathbf{y}$ axis
$\beta$	angle defining the insonification angle
$\gamma_{\kappa}$	relative contrast in compressibility
$\gamma_{\rho}$	relative contrast in density

TABLE II. The mean of QUS parameters estimated by the anisotropic or isotropic EMTLMA for the aggregating configurations consisting in perfectly aligned prolate ellipsoids at hematocrit  $\phi=30\%$ . Also given are the corresponding goodness-of-fit  $R^2$ .

	Actual aggregates parameters			QUS parameters estimated by EMTLMA					
				Anisotropic		Isotropic ( $\overline{BSC(\beta)}$ )		Isotropic ( $BSC(\beta = 0)$ )	
	$(\bar{b}/a, \sigma_b/a, \nu_f)$	$(\bar{r}_{eq}/a, \sigma_{eq}/a)$	$D_{iBSC}$	$(\bar{b}^*/a, \sigma_b^*/a, \nu_f^*)$	$R^2$	$(\bar{r}^*/a, \sigma_r^*/a)$	$R^2$	$(\bar{r}^*/a, \sigma_r^*/a)$	$R^2$
1	(2.50, 0.75, 1.5)	(2.86, 0.61)	0.55	(2.47, 0.75, 1.44)	0.97	(3.09, 0.73)	0.93	(3.27, 0.61)	0.89
2	(2.50, 0.75, 2.0)	(3.15, 0.95)	1.49	(2.45, 0.75, 1.93)	0.97	(3.42, 0.75)	0.80	(3.64, 0.55)	0.60
3	(2.50, 0.75, 2.5)	(3.39, 1.02)	3.06	(2.44, 0.72, 2.57)	0.98	(3.55, 0.82)	0.67	(3.80, 0.66)	0.25
4	(2.50, 0.45, 2.0)	(3.15, 0.57)	0.31	(2.44, 0.49, 1.94)	0.98	(3.27, 0.40)	0.96	(3.35, 0.17)	0.94
5	(2.50, 0.35, 2.0)	(3.15, 0.44)	0.26	(2.46, 0.42, 1.80)	0.98	(3.17, 0.33)	0.98	(3.16, 0.24)	0.97
6	(2.50, 0.18, 2.0)	(3.15, 0.22)	0.46	(2.44, 0.18, 2.03)	0.99	(3.08, 0.23)	0.99	(2.98, 0.24)	0.98

TABLE III. The mean values of QUS parameters estimated by the anisotropic or isotropic EMTLMA for hematocrits of 10% and 30% when considering the complex aggregating configurations with blood sample A (see lines 1 and 2) and sample B (see lines 3 and 4). Also given are the corresponding goodness-of-fit  $R^2$ .

	Actual aggregates parameters			QUS parameters estimated by EMTLMA							
	$\phi$	$(\bar{b}/a, \sigma_b/a, \nu_f)$	$(\bar{r}_{eq}/a, \sigma_{eq}/a)$	$D_{iBSC}$	Anisotropic			Isotropic ( $\overline{BSC(\beta)}$ )		Isotropic ( $BSC(\beta = 0)$ )	
					$(\bar{b}^*/a, \sigma_b^*/a, \nu_f^*)$	$(\bar{r}^*/a, \sigma_r^*/a)$	$R^2$	$(\bar{r}^*/a, \sigma_r^*/a)$	$R^2$	$(\bar{r}^*/a, \sigma_r^*/a)$	$R^2$
1	10%	(2.61, 0.59, 2.7)	(3.56, 0.78)	2.49	(2.81, 0.76, 1.40)	(3.14, 0.83)	0.85	(3.13, 0.72)	0.95	(3.49, 0.33)	0.87
2	30%	(2.61, 0.59, 2.7)	(3.56, 0.78)	1.25	(2.76, 0.74, 1.39)	(3.08, 0.81)	0.88	(2.93, 0.82)	0.96	(3.25, 0.67)	0.91
3	10%	(2.26, 0.55, 2.0)	(2.79, 0.70)	0.75	(2.59, 0.66, 1.00)	(2.59, 0.66)	0.90	(2.59, 0.66)	0.98	(2.65, 0.62)	0.98
4	30%	(2.26, 0.55, 2.0)	(2.79, 0.70)	0.68	(2.59, 0.64, 1.00)	(2.59, 0.64)	0.93	(2.58, 0.65)	0.97	(2.59, 0.64)	0.98